INDUSTRIAL ROBOTS

Inverted and vertical climbing of a quadrupedal microrobot using electroadhesion

Sébastien D. de Rivaz, Benjamin Goldberg, Neel Doshi, Kaushik Jayaram, Jack Zhou, Robert J. Wood*

Copyright © 2018 The Authors, some rights reserved; exclusive licensee American Association for the Advancement of Science. No claim to original U.S. Government Works

The ability to climb greatly increases the reachable workspace of terrestrial robots, improving their utility for inspection and exploration tasks. This is particularly desirable for small (millimeter-scale) legged robots operating in confined environments. This paper presents a 1.48-gram and 4.5-centimeter-long tethered quadrupedal microrobot, the Harvard Ambulatory MicroRobot with Electroadhesion (HAMR-E). The design of HAMR-E enables precise leg motions and voltage-controlled electroadhesion for repeatable and reliable climbing of inverted and vertical surfaces. The innovations that enable this behavior are an integrated leg structure with electroadhesive pads and passive alignment ankles and a parametric tripedal crawling gait. At a relatively low adhesion voltage of 250 volts, HAMR-E achieves speeds up to 1.2 (4.6) millimeters per second and can ambulate for a maximum of 215 (162) steps during vertical (inverted) locomotion. Furthermore, HAMR-E still retains the ability for high-speed locomotion at 140 millimeters per second on horizontal surfaces. As a demonstration of its potential for industrial applications, such as in situ inspection of high-value assets, we show that HAMR-E is capable of achieving open-loop, inverted locomotion inside a curved portion of a commercial jet engine.

INTRODUCTION

Natural and man-made terrains often contain steep inclines, walls, and overhangs. To successfully and efficiently navigate in these complex and unstructured environments, a legged robot must have mechanisms and gaits that enable multiple locomotion modalities (e.g., running, climbing, or jumping), especially in confined environments (*1*). Specifically, millimeter-scale climbing robots can explore three-dimensional (3D) environments and have the benefit that weight-specific adhesion becomes higher as the robot's size decreases when using area-dependent adhesion mechanisms (i.e., electroadhesion and dry adhesives). The combination of increased weight-specific adhesion and reduced size makes climbing microrobots strong candidates for inspection and exploration tasks (*2*).

Notable previous work on inclined legged locomotion has focused on adapting adhesion mechanisms inspired by nature's best climbers (*3*). Gecko-inspired dry adhesion (*4*, *5*) has been used by numerous climbing robots both large (*6*–*10*) and small (*11*, *12*) to scale a variety of smooth inclined surfaces. Similarly, robots relying on insect-inspired microspine attachments (*13*, *14*) have been particularly effective at rapidly climbing vertical textured surfaces. These robots, however, face difficulties during inverted climbing due to the requirement of generating large shear forces to maintain normal adhesion.

In parallel with bioinspired adhesion strategies, engineered methods, such as vacuum tracks (*15*, *16*), permanent magnetic and electromagnetic mechanisms (*17*, *18*), and electroadhesive pads (*19*–*21*), have proven to be successful surface attachment options. It is often the case that the adhesion type determines the size and design complexity of the robot; for example, vacuum track–based suction mechanisms (*15*, *16*) or electromagnetic mechanisms (*17*, *18*) require the robots to use heavy on-board components that increase their overall mass and reduce maneuverability. In contrast to these methods, electroadhesion is lightweight and has several advantages for use in a legged, climbing microrobot. First, repeatable engagement and disengagement are easily achieved by switching the applied electric field. Therefore, the addition of such an adhesion mechanism, in principle, requires minimal modifications to the locomotion (gait) strategy and enables operation with and without electroadhesion. Second, the generated adhesion force is easily tuned via input voltage modulation and consumes low power (*22*) while engaging with diverse surface types. Last, electroadhesion is especially well suited for engineered (conductive) surfaces, because it requires simple pad geometries, is easily switchable, and results in robust adhesion at relatively low voltages.

This paper presents the Harvard Ambulatory MicroRobot with Electroadhesion (HAMR-E; Fig. 1): a 1.48-g, 4.5-cm-long tethered quadrupedal climbing microrobot. HAMR-E uses origami-based design and the printed-circuit micro-electromechanical systems (PC-MEMS) manufacturing processes (*23*) to achieve structural and functional complexity similar to that of large legged climbing robots such as Stickybot [370 g (*6*)] and RiSE [3.8 kg (*24*)]. Furthermore, HAMR-E leverages its small form factor to achieve high weight-specific adhesion. One key contribution described in this paper that enables robust locomotion at arbitrary inclines is the integration and characterization of low-voltage electroadhesive pads and passive origami ankles. Another innovation is the design and tuning of a parametric tripedal crawl gait. Last, we performed extensive experiments to evaluate these newly designed elements and the robot's locomotion performance. Our studies demonstrate that HAMR-E is one of the smallest legged robots capable of versatile locomotion on arbitrarily inclined and curved "real-world" conductive surfaces.

RESULTS

We based our climbing microrobot (Fig. 2A) on the Harvard Ambulatory MicroRobot (HAMR-VI), a 1.43-g quadruped that is capable of high-speed running (*25*), climbing (*26*), and power and control autonomy (*27*). The robot has eight degrees of freedom (DOFs) actuated by high–power density piezoelectric bending bimorph actuators (*28*). A spherical five-bar (SFB) transmission connects the two actuators to a single leg for independent control of swing (leg-x) and lift (leg-z) motions (fig. S1). The SFB transmission and actuators are sized as

John A. Paulson School of Engineering and Applied Sciences and Wyss Institute for Biologically Inspired Engineering, Harvard University, Cambridge, MA 02138, USA.
*Corresponding author. Email: rjwood@seas.harvard.edu

Downloaded from https://www.science.org at The Hong Kong University of Science and Technology (Guangzhou) on May 26, 2026

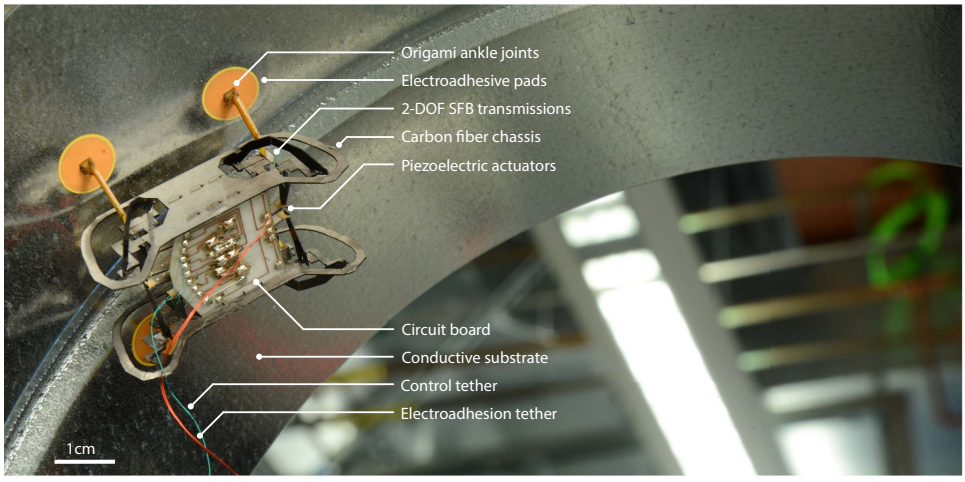

Fig. 1. HAMR-E performing inverted locomotion. Manufactured using PC-MEMS techniques (*23*), HAMR-E is an insect-scale legged robot that combines electroadhesion and a highly articulated drive train to enable locomotion on inclines from 0° to 180°.

described in (*29*) to provide sufficient force for inverted and vertical locomotion.

The key contributions of this work are described in the following sections. The design and evaluation of the integrated leg structure are described in the next section, and the development of the parametric tripedal crawl gait is detailed in the "Gait design" section. These advances were leveraged to demonstrate horizontal, vertical, and inverted locomotion on conductive surfaces ("Locomotion characterization").

Integrated leg structure design

Inverted and vertical locomotion requires normal and shear adhesion forces at least equal to the robot's body weight. To satisfy these requirements, we developed a functional leg (electroadhesive footpad and passive origami ankle; Fig. 2B) that provides robust adhesion for inverted and vertical locomotion while retaining horizontal running capabilities.

Low-voltage, electroadhesive footpads

We leveraged insights from previous work with electroadhesion in microrobots (*26*, *30*) to develop a suitable footpad for HAMR. Using a standard model for electroadhesion (*31*), the adhesion force generated by an electrode on a conductive substrate is given by

$$F_{\mathrm{adh}} = A\varepsilon_0\varepsilon_{\mathrm{d}}\frac{V^2}{2d^2} = A\varepsilon_0\varepsilon_{\mathrm{d}}\frac{E^2}{2} \quad (1)$$

where A is the electrode area, ε_0 is the permittivity of vacuum, ε_{d} is the dielectric constant of the dielectric material, V is the applied voltage differential, d is the dielectric thickness, and $E = V/d$ is the applied electric field. Intuitively, the footpad and conductive substrate form a parallel plate capacitor, and F_{adh} is the attractive force between the plates. The Coulomb friction model states that the maximum shear force the footpad can support is

$$F_{\mathrm{shear}} = \mu F_{\mathrm{adh}} \quad (2)$$

where μ is the coefficient of static friction between the footpad and the conductive substrate.

For such footpads (Fig. 2B), the two major design considerations are the choices of electrode geometry and dielectric material. Although electrode design for engagement to arbitrary substrates is an active area of research (*22*, *31*, *32*), the solution is more straightforward for conductive substrates. Adhesion force is governed by the area (linearly increases; Eq. 1) of the electrodes. To simplify their geometry, we considered only circular electrodes because they mitigate electric field concentrations near the edges and avoided preferential bending axes after repeated use. The selection of dielectric material was dictated by trade-offs between minimizing the thickness and maximizing the dielectric constant, the coefficient of friction (Eq. 2), and the electrical breakdown voltage.

We evaluated the maximum shear force supported by footpads with varying geometries and dielectric materials (see Materials and Methods for details). The experimental measurements and theoretical predictions (Eq. 2) of maximum shear adhesion as a function of applied field are shown in fig. S2 for a variety of pad designs. Similar measurements for the best two footpads, with polyimide and silicone dielectrics, are shown in Fig. 2C. We found that polyimide dielectric ($\varepsilon_{\mathrm{d}} = 3.5$) footpads generated normal adhesion comparable with silicone versions ($\varepsilon_{\mathrm{d}} = 2.7$). Furthermore, footpads with a silicone dielectric ($\mu = 0.75$) generated larger shear adhesion than those with a polyimide dielectric ($\mu = 0.25$) at the same field strength. However, the silicone pads suffered from dielectric breakdown within the desired operating voltages ($\leq$300 V) because of the significantly lower dielectric strength of silicone ($E_{\mathrm{max}} \approx 20$ V μm^{-1}) compared with polyimide ($E_{\mathrm{max}} \approx 120$ V μm^{-1}). We also explored a hybrid footpad (fig. S2D); however, fabrication challenges limited the overall thickness to 21 μm, resulting in reduced overall adhesion force.

On the basis of the above results, the electrodes for HAMR-E have a radius of 4.5 mm and a 12.5-μm-thick polyimide dielectric. An individual pad is designed to generate 3.25 g of shear force for a high factor of safety during climbing at an adhesion voltage of 250 V. These footpads are also theoretically able to withstand up to ~1600 V, providing a substantial margin for operation at higher voltages if needed. However, a voltage of 250 V was targeted, because it is comparable with the actuator drive voltages and would allow for shared use of high-voltage components in a power-autonomous version.

In addition to the previously discussed design choices (electrode geometry and dielectric material), we expected the overall stiffness of the footpad to play an important role in determining its effectiveness. Complaint footpads conform better to a substrate, maximizing their effective contact area and increasing adhesion. A 0.2-μm copper electrode with a 12.5-μm acrylic adhesive backing was used in the footpad to provide a balance between low stiffness and resistance to plastic deformation. As shown in Discussion, these compliant footpads could enable locomotion even on surfaces with moderate local curvature.

Last, the estimated capacitance for our footpads is 160 pF. The typical line resistance for the circuitry driving the pads is 1 kilohm. This results in a time constant of 160 ns. In addition, we determined that the time constant for the entire electrical system (DC-DC amplifier in series

Downloaded from https://www.science.org at The Hong Kong University of Science and Technology (Guangzhou) on May 26, 2026

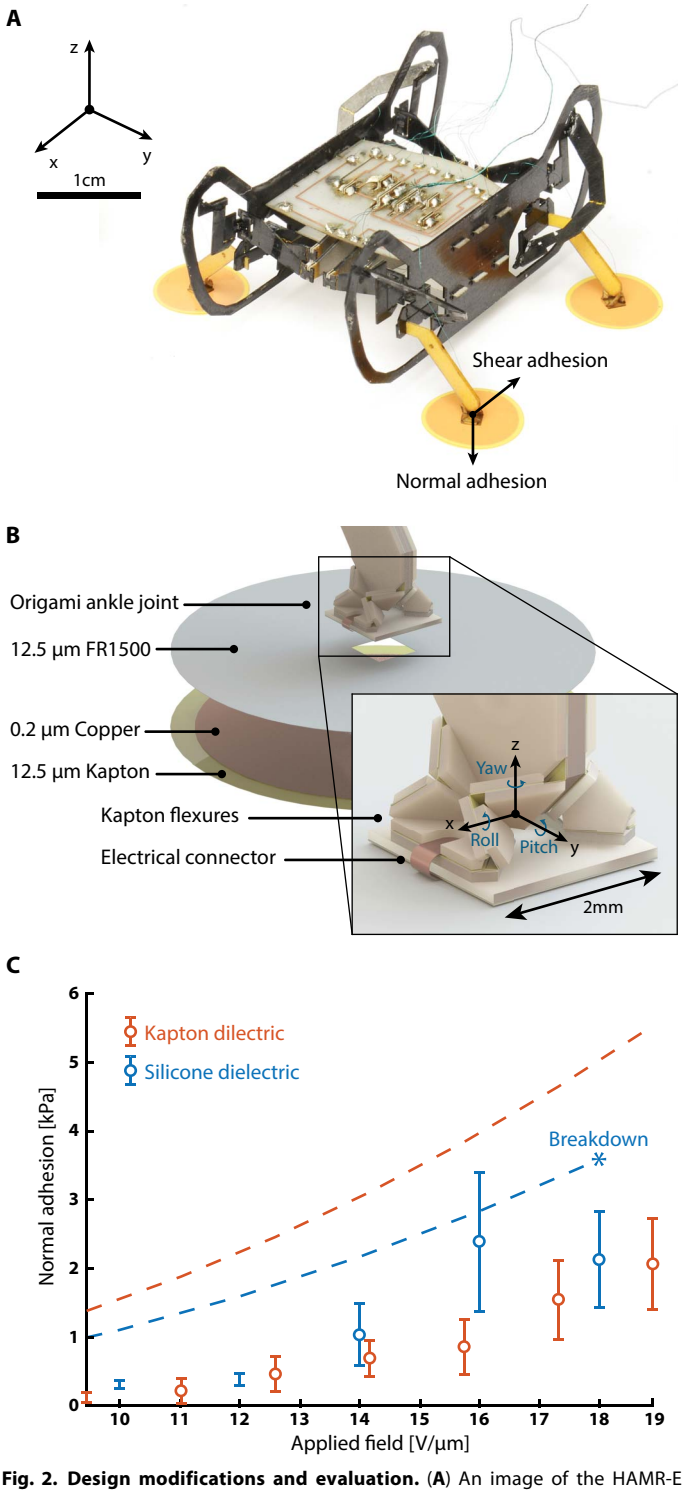

Fig. 2. Design modifications and evaluation. (**A**) An image of the HAMR-E including axes definitions. (**B**) Schematic representation of the electroadhesive pad and the three-DOF origami ankle with components labeled. Inset depicts a detailed view of the ankle's center of rotation. (**C**) Experimental (mean ± SD, $n = 5$) and theoretical normal adhesion pressure as a function of applied electrical field for the highest-performing pad designs (see fig. S2 for measurement details).

with a pad; fig. S5B) is approximately 2.6 ± 0.5 ms ($n = 8$ trials, two pads). Representative voltage traces during charge and discharge are shown in fig. S7 (A and B, respectively). The system time constant is likely dominated by that of the DC-DC amplifier and is too small to affect pad performance at typical operating frequencies (0.2 to 2 Hz).

Passive ankles

The footpad described in the previous section was attached to a passive three-DOF origami ankle joint located at the distal tip of the leg (Fig. 2B). These ankles (*26*) compensated for leg rotations induced by the transmission kinematics and body dynamics. In addition, the ankles also passively aligned to macroscale surface topology, increasing effective contact area. Each ankle joint is composed of 12 flexures embedded into the monolithic leg structure fabricated with the PC-MEMS processes. The laminate was then folded up into its final configuration in an origami-like fashion.

The kinematics of the ankle allowed for leg rotations of ±90° in roll and ±45° in pitch and yaw. Ideal ankles should behave like perfect ball joints that transmit only forces and no moments. To meet this requirement, we chose 7.5-μm polyimide as our flexure material because it provided the lowest stiffness while maintaining structural integrity (i.e., without tearing). During the stance phase of locomotion, the legs rotated about the yaw axis, inducing an equivalent passive rotation in the ankles without visible changes in the orientation of the footpad (movie S4), that was quantified to be approximately 30°.

Static performance characterization

We quantified the robot's static factor of safety by experimentally determining the maximum applied normal and shear load before pad disengagement. We applied these loads near the robot's center of mass (COM) to replicate the effects of gravity. We measured a maximum shear load of 5.56 ± 1.30 g ($n = 6$) and a maximum normal load of 6.20 ± 0.6 g ($n = 6$) before pad disengagement. These measured loads are smaller than four times the normal or shear adhesion generated by a single pad because of susceptibility of these pads under peeling loads (*30*). However, these values still result in static factors of safety of 4.2 and 3.7 for inverted and vertical locomotion, respectively.

Gait design

Appropriate gait patterns have enabled diverse climbing strategies (*33*), including pole climbing (*34*), dynamic climbing (*35*), and electroadhesive climbing (*19*). Traditionally, however, legged climbers are hexapedal (*6*, *36*) and use a tripedal crawl gait (*37*) that provides three points of contact for static stability. After these studies, we developed a tripedal gait for our quadrupedal morphology (Fig. 3) that guaranteed static stability, increased normal adhesion compared with a balanced diagonal gait, and provided more freedom to adjust the robot's position and orientation during locomotion.

Gait definition

During a single cycle of our tripedal crawl, the feet swung forward (Fig. 3A) in the following order: front-left (blue), rear-right (red), front-right (green), and rear-left (yellow). The voltage signals sent to a pair of feet are shown in Fig. 3 (B to D). The electroadhesion voltage signal (Fig. 3B) was binary and inactive for 18% of the cycle, whereas the corresponding leg was in the swing phase. The duration of a leg's swing phase was determined by the swing duty cycle (DC), which was set to less than

Downloaded from https://www.science.org at The Hong Kong University of Science and Technology (Guangzhou) on May 26, 2026

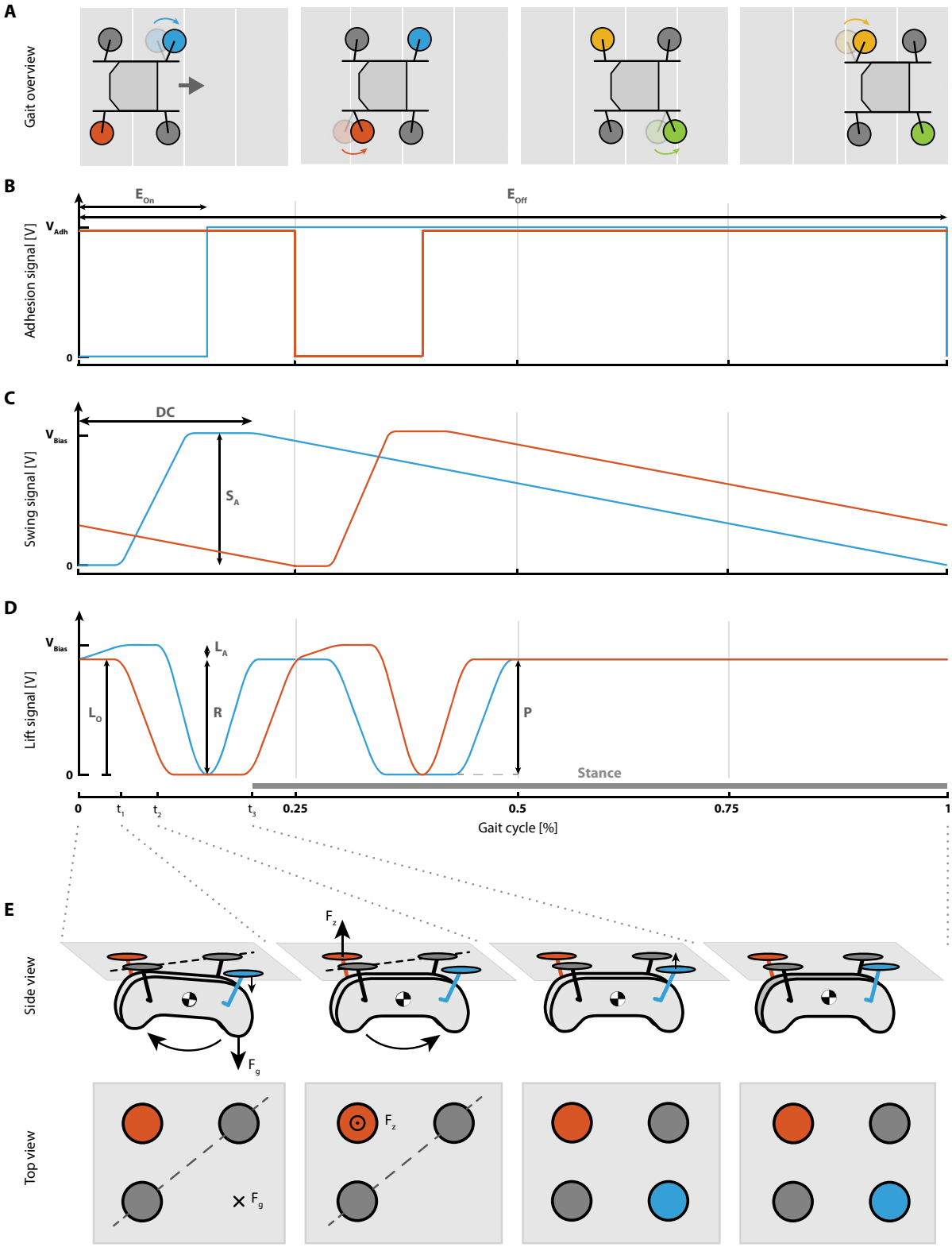

Fig. 3. Modified tripedal crawl gait. (**A**) Schematic representation of the tripedal crawl gait with individual legs colored. Footfalls are spaced one-quarter cycle apart. (**B**) Electroadhesion input voltage for consecutive legs, characterized by the activation (E_{On}) and deactivation (E_{Off}) timings. Note that the orange signal is artificially offset for clarity. (**C**) Swing input voltage for the newly designed gait with duty cycle (DC) and swing amplitude S_A labeled. (**D**) Lift input voltage for the newly designed gait defined by the lift offset (L_O), the lift amplitude (L_A), reach (R), and push (P) parameters. (**E**) Schematics of HAMR-E's pose and gait pattern visualizing the effects of the reach and push parameters during a quarter gait cycle.

Downloaded from https://www.science.org at The Hong Kong University of Science and Technology (Guangzhou) on May 26, 2026

a quarter of the period to guarantee a tripod of support at all times. Each leg's swing amplitude (S_A) was set to its full capacity to maximize forward velocity. The lift voltage is defined by an initial bias (L_O) that brings the body COM as close to the substrate as possible while leaving sufficient margin (L_A) to disengage the pads. The exact values of these parameters are listed in table S1.

In addition, the lift voltage was determined by two more parameters that modulate the generation of body torques to oppose rotations induced by gravity during inverted locomotion: reach (R) and push (P) (Fig. 3C). These parameters were defined as a percentage of the maximum available displacement. The reach parameter modulated the vertical (lift) displacement of the active leg as it was lowered toward the substrate, and the push parameter governed the normal force generated by the diagonally opposite leg as it pushed on the substrate. The reach parameter ensured that the active leg contacts the climbing plane without reaching too far and generating destabilizing torques, and the push parameter induced a torque about the robot's diagonal axis to compensate for rotations during pad disengagement.

In summary, an ideal cycle (Fig. 3E) started with all four feet in contact with the substrate (t = 0, Fig. 3E). Before each active leg's swing cycle, adhesion was disabled for that foot ($t_1 \rightarrow t_2$). To compensate for destabilizing gravitational forces after pad detachment, we applied a restoring torque before the swing cycle by pushing against the substrate with the diagonally opposite leg (push, $t_2 \rightarrow t_3$). Last, the active leg adhered to the climbing plane after having swung forward (reach, $t_3 \rightarrow 0.25$). This process was then repeated for the other three legs in a full cycle. To turn, the above gait definition was maintained with one exception—the swing amplitude was set to zero (S_A = 0) on the two inside legs during locomotion.

Experimental gait tuning

We experimentally tuned the reach and push parameters to maximize the number of steps achieved using a feed-forward gait strategy, because it is not feasible to achieve an indefinite number of steps without feedback control (see Discussion). Furthermore, the number of open-loop steps serves as a useful quantitative metric for comparing the

Downloaded from https://www.science.org at The Hong Kong University of Science and Technology (Guangzhou) on May 26, 2026

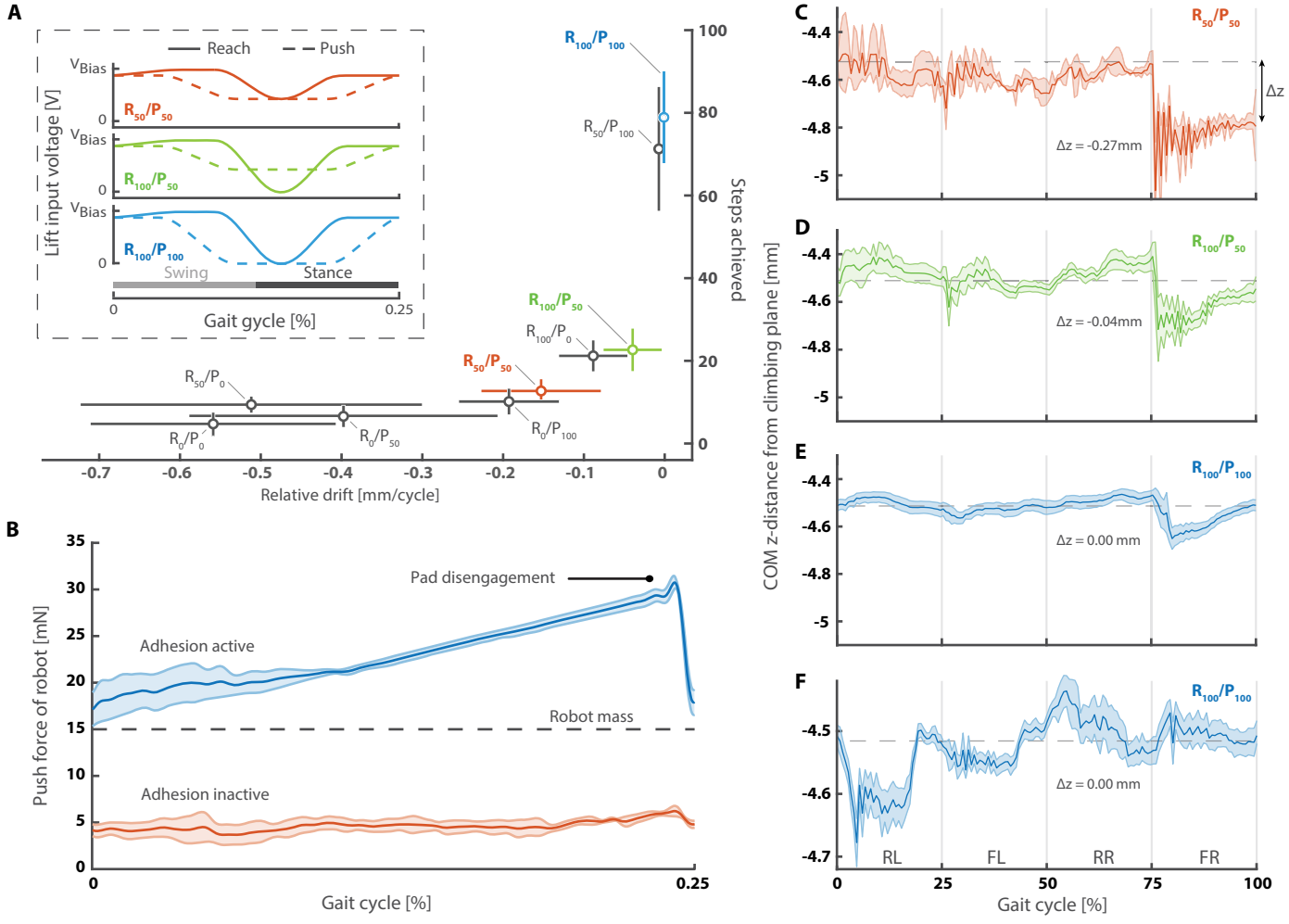

Fig. 4. Experimental gait tuning results. (**A**) Drift in COM height versus cycles achieved for nine different combinations of reach and push parameters. Error bars represent ±1 SD (n = 5). The inset shows the modifications to the lift actuator inputs for the reach and push parameters. (**B**) Push force measurements during the tripedal crawl with (blue) and without (red) electroadhesion active. Shaded regions show ±1 SE (n = 5). (**C** to **E**) COM height during the gait cycle for different reach and push parameter combinations: R_{50}/P_{50}, R_{100}/P_{50}, and R_{100}/P_{100} during inverted locomotion. Shaded regions represent ±1 SD (n = 3 trials with 6, 12, and 40 cycles, respectively). (**F**) COM height during vertical locomotion for the R_{100}/P_{100} gait. Shaded region represents ±1 SD (n = 40).

influence of the reach and push parameters. A total of nine different waveforms (table S1), defined by combinations of 0, 50, or 100% values of reach and push, were evaluated. We found that these parameters were critical to achieving sustained inverted locomotion, because increasing them reduced the relative drift between the COM and substrate and increased the number of open-loop steps achieved (Fig. 4A).

For example, the robot was only able to perform open-loop inverted locomotion for fewer than eight steps on average (movie S6) when using a R_0/P_0 tripedal crawl since the COM falls 600 μm per cycle. On the

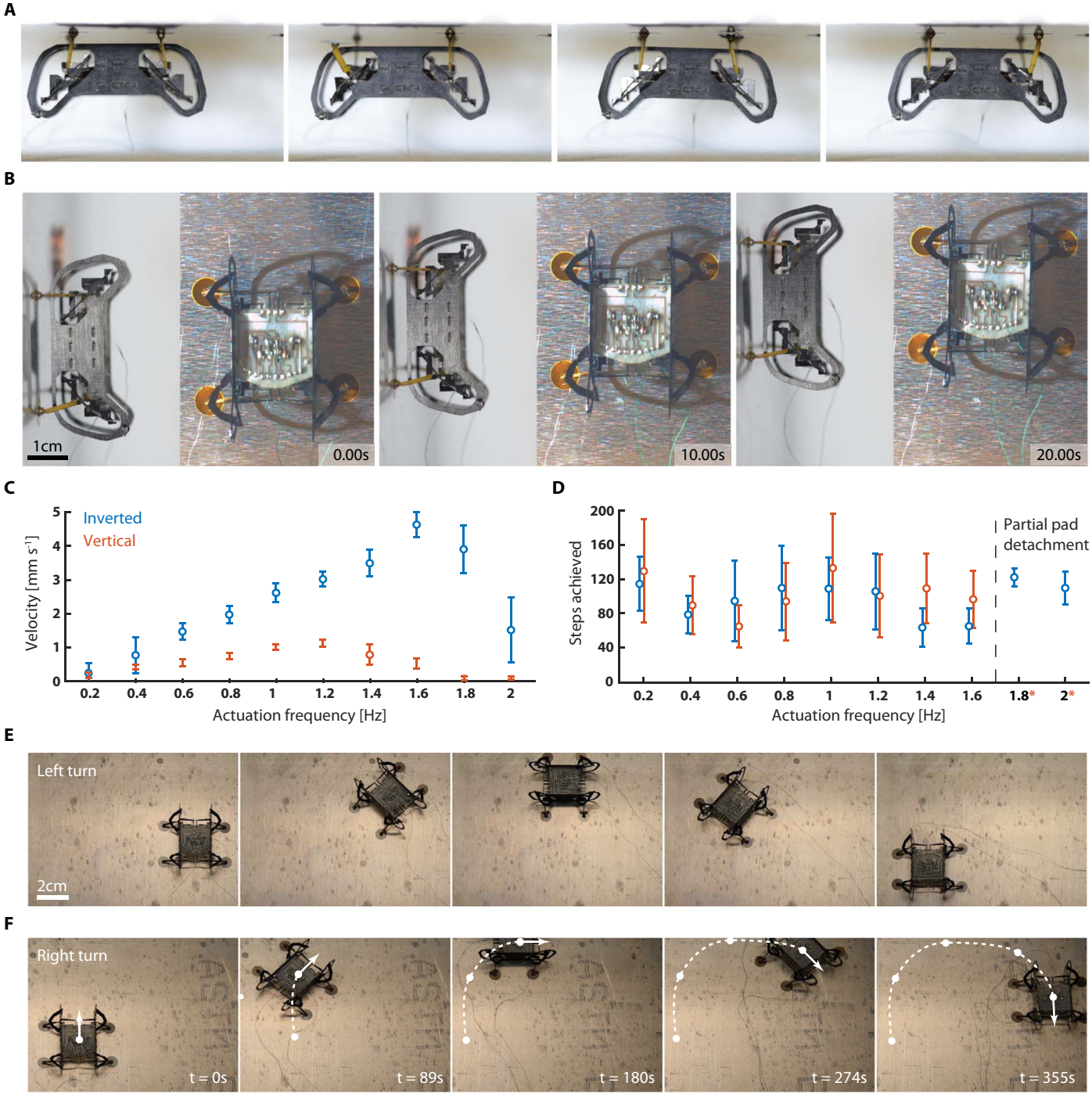

Fig. 5. Locomotion performance on inverted and vertical surfaces, and during left and right maneuvers. Time-stamped images of HAMR-E performing inverted (**A**) and vertical (**B**) locomotion at a stride frequency of 0.2 Hz. (**C**) Average forward velocity (mean ± SD, $n = 5$) as a function of frequency during inverted (blue) and vertical (orange) locomotion. (**D**) Number of open-loop steps achieved (mean ± SD, $n = 5$) as a function of stride frequency. Pads failed to completely disengage from the substrate at frequencies higher than 1.6 Hz during vertical locomotion, resulting in sustained locomotion (marked by an asterisk). Time-stamped images from a left (**E**) and right (**F**) turn using the tripedal crawl gait with electroadhesion active on a horizontal conductive substrate.

Downloaded from https://www.science.org at The Hong Kong University of Science and Technology (Guangzhou) on May 26, 2026

other hand, the COM drift was negligible when the reach and push parameters were both set to 100%, allowing the robot to achieve 80 steps on average. We also compared cycle-averaged time course data of the relative height of the robot's COM for the R_{50}/P_{50}, R_{100}/P_{50}, and R_{100}/P_{100} tripedal crawl gaits (Fig. 4, C to E). The R_{50}/P_{50} gait had a net COM drift of 0.27 mm per cycle compared with no measurable drift for the R_{100}/P_{100} gait (see fig. S4 for detailed drive signals). Furthermore, the mean-subtracted, root mean square (RMS) z height of the COM decreased with increasing values of the reach and push parameters, implying smoother locomotion with fewer oscillations. For example, RMS z oscillations were decreased from 0.09 to 0.04 mm with R_{50}/P_{50} and R_{100}/P_{100}, respectively.

Having tuned the tripedal crawl for inverted locomotion, we evaluated the best-performing gait (R_{100}/P_{100}) during vertical locomotion. We first measured the net thrust force produced during a single cycle by using the experimental setup described in the "Blocked force measurements" section. The robot exerted a maximum force of 3.1 g (Fig. 4B), which is only 20% lower than the maximum horizontal (swing) blocked force produced by three legs [3.9 g (*29*)]. In addition, the average force generated during stance was 2.4 ± 0.1 g, indicating that the R_{100}/P_{100} tripedal crawl could produce a net positive force during vertical locomotion. We found minimal COM drift away from the substrate during vertical locomotion (Fig. 4F) using the R_{100}/P_{100} tripedal crawl, indicating its suitability for vertical locomotion.

Locomotion characterization

Having identified a functional gait for inverted and vertical locomotion, we characterized various aspects of the robot's locomotion by using the experimental setup in Fig. 7C. These included the frequency dependence of the robot's performance on inverted and vertical surfaces, the robot's ability to walk on inverted inclines and horizontal surfaces, the robot's maneuverability, and its cost of transport.

Inverted and vertical locomotion

A series of time-stamped images of the robot during inverted locomotion with a stride frequency (f) of 0.2 Hz are presented in Fig. 5A (movie S1). The robot's velocity increased linearly with actuation frequency (Fig. 5C) until $f \simeq 1.6$ Hz, where it achieved a maximum speed of 4.6 mm s^{-1} [0.10 ± 0.1 body length (BL) s^{-1}]. The robot's velocity dropped rapidly after this point, likely because of body oscillations caused by the detachment of the pads under residual loading (see fig. S7D). The number of successful open-loop inverted steps (Fig. 5D) was roughly independent of stride frequency.

Similarly, time-stamped images of the robot during vertical locomotion with a stride frequency of 0.2 Hz are presented in Fig. 5B (movie S2). Like inverted locomotion, the robot's velocity increased linearly with actuation frequency (Fig. 5C) until $f \simeq 1.2$ Hz, where it achieved a maximum speed of 1.2 mm s^{-1} (0.026 ± 0.04 BL s^{-1}). We observed a similar velocity drop after 1.2 Hz. The number of successful open-loop vertical steps (Fig. 5D) was roughly independent of stride frequency up to 1.6 Hz, after which the pads failed to disengage from the substrate. We note that the maximum achievable velocity during vertical locomotion corresponded to about 25% of the maximum velocity during inverted locomotion. Gravitational forces acting against the direction of motion reduced the effective stride length during

Table 1. Climbing robots comparison. T, tethered; UT, untethered; N/A, not available.

Climbing robot	Adhesion strategy	BL (mm)	Robot mass (g)	Maximum voltage (V)	Incline range (°)	Maximum velocity for given incline (BL s^{-1})
HAMR-E, T	Electroadhesion	45	1.48	250	0–180	0°: 3.1 90°: 0.026 180°: 0.10
Electroadhesive climbing robots						
Wang *et al.* (*19*), T	Electroadhesion	183	49	100	0–90	0°: 0.58 90°: 0.56
Wang *et al.* (*51*), T	Electroadhesion	173	94	600	0–90	90°: 0.2
Prahlad *et al.* (*40*), T	Electroadhesion	400	180	4000	0–90	90°: 0.375
Yamamoto *et al.* (*39*), T	Electroadhesion	300	327	1500	0–90	90°: 0.022
Liu *et al.* (*20*), UT	Electroadhesion	360	700	3000	0–90	90°: <0.001
Other legged climbing robots < 100 g						
Hawkes *et al.* (*11*), T	Dry adhesion	12	0.02	N/A	0–90	Not reported
Hawkes *et al.* (*11*), UT	Dry adhesion	30	9	3.7	0–90	90°: 0.6
Greuter *et al.* (*10*), UT	Dry adhesion	40	10	3.7	0–90	90°: 0.08
Birkmeyer *et al.* (*52*), UT	Spines	100	15	3.7	0–90	90°: 1.5
Breckwoldt *et al.* (*12*), UT	Dry adhesion	47	22	3.7	0–180	90°: 1.6 180°: 1.8
Murphy *et al.* (*7*), UT	Dry adhesion	96	85	N/A	0–180	0°: 0.5 90°: 0.5 180°: 0.5

Downloaded from https://www.science.org at The Hong Kong University of Science and Technology (Guangzhou) on May 26, 2026

vertical locomotion to about 75% of forward displacement achieved during inverted locomotion (fig. S6).

Inverted incline and horizontal locomotion

To further highlight the versatility of HAMR-E's inclined locomotion capabilities, we demonstrated locomotion at a stride frequency of 1.0 Hz on an inverted incline (movie S3). In addition, we verified that the robot still retained horizontal locomotion capabilities comparable with HAMR-VI. Specifically, it achieved forward velocities of 7.5 to 140.4 mm s^{-1} with the trot gait over stride frequencies ranging from 2 to 65 Hz. Although these speeds, on average, are about 50% slower compared with HAMR-VI (*25*), the robot was still able to achieve a top speed of 3.1 BL s^{-1}, and further gait optimization could increase these speeds for both horizontal and climbing locomotion.

Maneuverability

With the gait strategy described earlier, we also demonstrated in-plane maneuverability by performing left and right turns during horizontal locomotion with active electroadhesion on a conductive surface (Fig. 5, E and F, and movie S7). By conducting the maneuverability studies on a horizontal surface, we avoided complications associated with failure via disengagement. At a stride frequency of 0.5 Hz, HAMR-E completed 180° left and right turns at speeds of 0.44° s^{-1} and 0.48° s^{-1}, respectively. The turning radii for these turns were 36.2 mm (0.80 BL) and 34.3 mm (0.76 BL). Although it took ~800 steps to complete a 180° turn, these open-loop turning strategies can easily be integrated with vertical or inverted locomotion once HAMR-E can walk indefinitely on these surfaces.

Cost of transport

Last, we also compared the robot's locomotive efficiency in different environments by calculating the cost of transport (CoT):

$$\mathrm{CoT} = \frac{P_{\mathrm{avg}}}{mgv_{\mathrm{avg}}} \tag{3}$$

where P_{avg} is the average electrical power consumed by the robot, v_{avg} is the robot's average speed, m is the robot's mass, and g is the acceleration due to gravity. This electrical power was consumed by both the actuators and electroadhesive pads (note S1), and details of the robot's power consumption and CoT during inverted and vertical locomotion are given in table S2. We found that the electroadhesive pads accounted for less than 10% of the total power, indicating that they did not significantly increase the robot's CoT. Furthermore, the overall CoT for HAMR-E is comparable with previous measurements for HAMR (*38*), and small discrepancies arose from a combination of manufacturing differences and differences in the actuator drive signals.

DISCUSSION

Here, we present a 1.48-g, 45 mm–by–40 mm–by–20 mm legged microrobot capable of locomotion on horizontal, vertical, and inverted conductive surfaces using electroadhesive pads. Adhesion to these surfaces is achieved at an operating voltage of 250 V, which is relatively low compared with previous studies (Table 1). Furthermore,

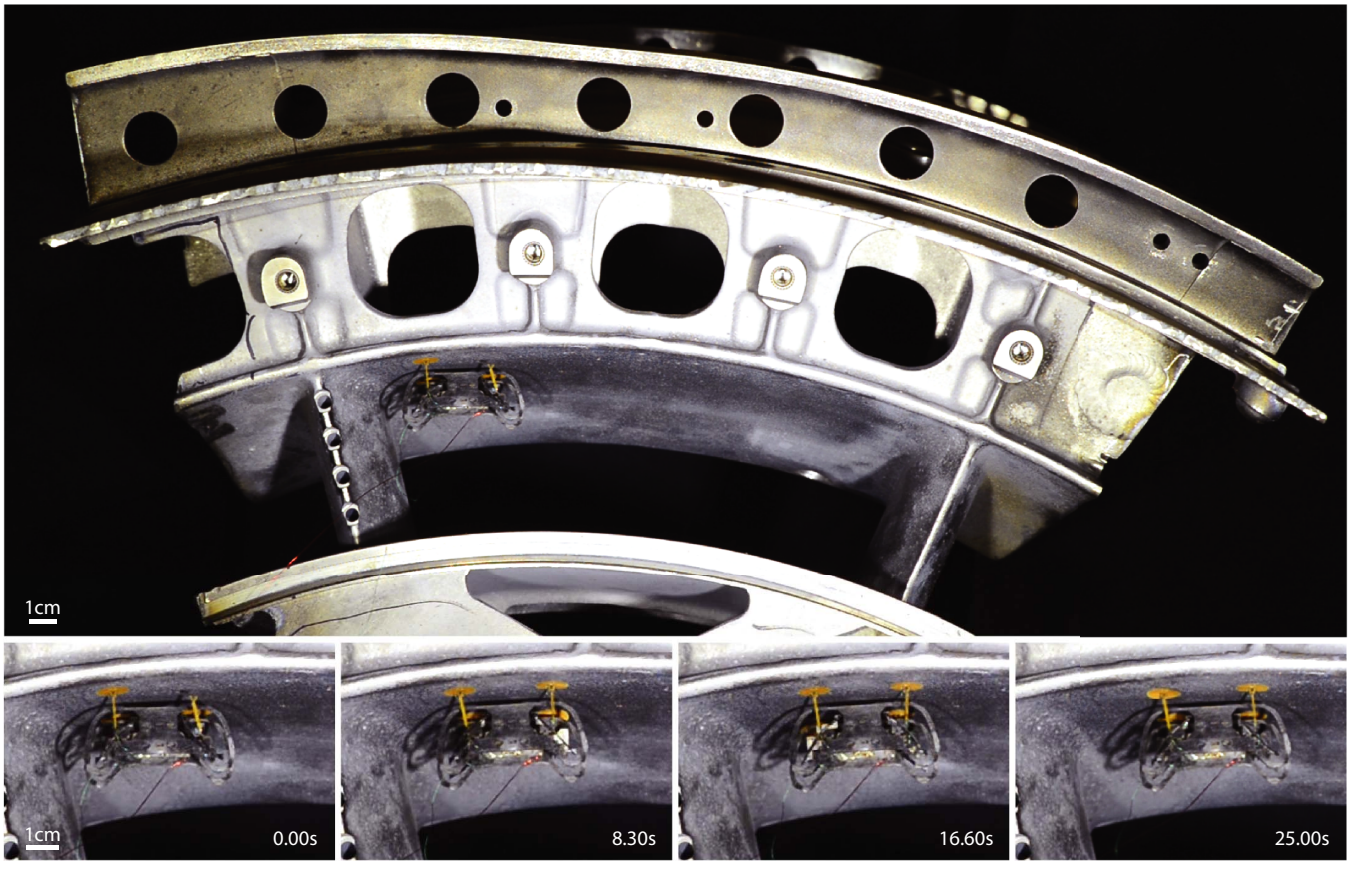

Fig. 6. Inverted locomotion on the inner surface of a commercial jet engine. This environment exhibits moderate local curvature and high surface roughness.

Downloaded from https://www.science.org at The Hong Kong University of Science and Technology (Guangzhou) on May 26, 2026

we demonstrated that electroadhesion consumed relatively little power compared with the actuators and there was only a small increase in the robot's cost of transport. We also developed a parametric tripedal crawl gait that can easily be adapted to other legged robots. Using this gait, we demonstrated that HAMR-E was capable of achieving more than 100 open-loop steps during inverted and vertical locomotion.

Table 1 shows a comparison of HAMR-E with other climbing robots in terms of BL, robot mass, adhesion strategy, operating voltage, incline range, and maximum achievable velocity. Our robot, like most other electroadhesive robots, is tethered; however, HAMR-E stands out from the other climbing robots in that it is one of the smallest legged climbing robots (mass of 1.48 g) that is capable of locomotion on arbitrary inclines. Most other small climbing robots [e.g., (*10*, *11*)] implement dry adhesion and thus have highly varied morphologies compared with HAMR-E. Compared with these robots, an advantage of the quadrupedal morphology and easily controllable adhesion of HAMR-E is that it lends itself nicely to being a generalist with the ability to customize and adapt gait.

In terms of vertical locomotion performance, our robot achieved speeds comparable with other electroadhesive legged robots (*20*, *39*) but was slower than electroadhesive wheeled or treaded robots (*19*, *40*). Similarly, the robot's locomotion performance on inclines was typically slower than other small legged climbing robots using passive adhesion mechanisms such as dry adhesion and microspines, which benefit from specialized foot and body designs. However, during locomotion on horizontal surfaces, HAMR-E achieved higher forward velocities compared with other climbing robots, which have body morphologies specialized for the adhesion mechanism of choice. The robot's rapid-running ability is a consequence of our decision to develop a module for surface attachment (via electroadhesive footpads) that allowed HAMR-E to retain many of the desirable features from successful earlier versions (*25*, *29*, *41*). This means that, despite being one of the smallest legged robots, HAMR-E is a highly capable and versatile robot that has the potential to adapt to varying terrains (*42*), change gaits to maximize speeds (*43*), exploit in-plane maneuverability (*44*), and achieve autonomous locomotion (*27*).

A target application for HAMR-E is to locomote within confined machinery for inspection purposes. The following paragraphs describe a potential application for HAMR-E within the aviation industry. Inspection of critical areas of jet engines is traditionally carried out through the use of human-operated borescopes with visual feedback. This process requires specially trained technicians and can result in an expensive engine removal if components under inspection do not conform to the safety criteria. Nonrotating components are particularly difficult to properly inspect with current tools, because the target object in question can be far away from the tool entry point into the engine. HAMR-E may provide a low-cost and time-efficient alternative, because it is similar in size to the inspection ports and is able to maneuver within the confined spaces of an engine (Fig. 6).

As a demonstration of a potential application for engine inspection, we performed open-loop locomotion on a curved-inverted surface in one of the critical sections of a jet engine (Fig. 6 and movie S5). Equipped with electroadhesion, alignment ankles, and a robust gait, HAMR-E is well suited to handle this challenging terrain. The surface is largely conductive, which is good for electroadhesion; however, the surface is also rough and curved and contains material impurities. Despite this, the robot was able to compensate by simply increasing the voltage to 600 V and having the ankles passively adapt to the curved surface without having to modify the gait parameters.

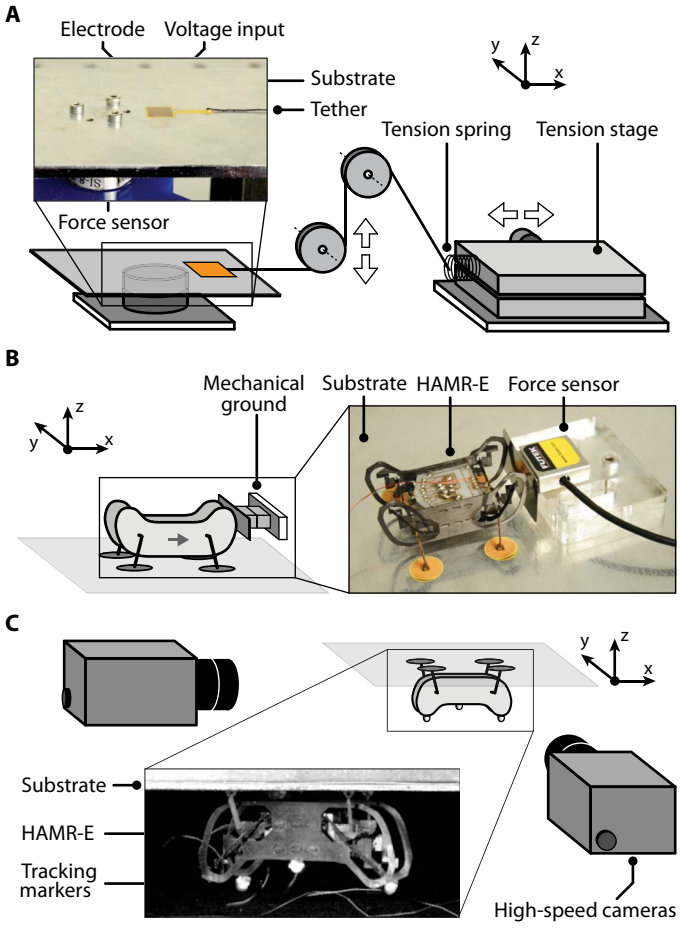

Fig. 7. Experimental setup for electroadhesive force measurements, blocked force measurement, and tracking of HAMR-E. (**A**) Schematic of the experimental setup used to measure the shear force generated by individual pads and both the shear and normal force generated by the whole robot. Components are labeled, and a detailed image of the pad attached to the substrate is shown. (**B**) Schematic of the experimental setup used to measure the push force generated by the whole robot. Components are labeled, and a detailed image of the robot pushing on the force sensor is shown. (**C**) Schematic of the experimental setup used to track the robot during inverted, vertical, and horizontal locomotion with components labeled. Two orthogonal high-speed cameras are centered on HAMR-E. Three reflective markers were placed on the robot (shown in the inset) and tracked by using vision-based techniques.

Although HAMR-E can climb a variety of challenging surfaces, occasional pad detachments prevented indefinite inverted and vertical locomotion. We found the effect of charge accumulation (a common cause of failure on nonconductive surfaces) to be negligible because the average disengagement force remained relatively constant over 120 cycles (fig. S7, C to E, and note S2). Consequently, we hypothesize that these failures can be attributed to a combination of state-dependent and stochastic effects, including creep in the polyimide flexures of the robot's transmissions, asperities in the climbing substrate, and external perturbations (e.g., interference from the tether and imperfect leg disengagement). To overcome such failures, we believe that closed-loop recovery strategies incorporating sensing technologies are likely to be most effective. Candidate sensors include piezoelectric encoders to measure leg position (*45*) and capacitive sensing (between the pads and the

Downloaded from https://www.science.org at The Hong Kong University of Science and Technology (Guangzhou) on May 26, 2026

substrate) to detect foot engagement. With this sensory information, a potential recovery strategy is one that resets the robot's COM back to its neutral position when a missed step is detected.

Immediate next steps intended to enhance HAMR-E's locomotion capabilities can take a number of directions, and a few of them are listed below. For example, further optimization of the drive train using techniques described in (*29*) could improve payload capacity and enable autonomous locomotion as in (*27*). Furthermore, our low-voltage electroadhesive footpads can share a high-voltage source with the actuators; consequently, integration with the autonomous HAMR (*27*) will require minimal modifications to the existing on-board drive electronics. The experimental strategy described above can also be used to optimize the climbing gait for the additional payload, because our footpads enable safety margins of 2.4× during vertical locomotion and 2.7× during inverted locomotion. Similarly, morphological changes—including adding additional legs, compliance in the backbone (*46*), and/or an active tail (*6*, *7*)—could help increase overall robustness to missed steps. Using the above mechanisms in concert with the tuned robot dynamics (*47*) could enable surface transitions to further increase performance. In parallel, optimizing the electroadhesive pad design for adhesion to nonconductive substrates (*30*) and investigating hybrid adhesion mechanisms (*48*) could increase the potential real-world applications. Last, we plan to study the robot's dynamics during inverted and vertical locomotion and use motion planning following the procedure in (*42*) to explore alternative gaits for climbing and increase HAMR-E's stability and speed. Ultimately, we hope that these improvements can one day allow microrobots to seamlessly navigate complex 3D surfaces much like their biological counterparts.

MATERIALS AND METHODS

Control and electroadhesion waveform generation

HAMR-E's eight piezoelectric actuators were operated in a unipolar drive configuration described in (*49*). Actuator signals were generated off-board at 1 kHz with a controller written in Simulink and interfaced with an xPC Target real-time testing environment (fig. S5). The actuator signals were then amplified to a maximum of 250 V, and electroadhesion signals were amplified up to 1000 V by using custom electronics (DC-DC converters, EMCO, AG Series; fig. S5B).

Electroadhesive pad fabrication

The silicone dielectric footpad is a four-layer composite laminate (fig. S3A). The insulation (or backing) consists of a layer of 12.5-μm acrylic adhesive (DuPont, Pyralux FR1500) laminated with heat and pressure to a 7.5-μm polyimide film (DuPont, Kapton). The electrode is a 200-nm layer of copper that was sputter-coated (Denton, Desktop Pro) onto the adhesive. Last, the dielectric is a layer of uncured silicone epoxy that was screen-printed onto the electrode and cured for 1 hour at 60°C.

The polyimide dielectric footpad is a three-layer composite laminate (fig. S3B). The dielectric is a 12.5-μm polyimide film (DuPont, Kapton), and the electrode is a 200-nm layer of copper that was sputter-coated (Denton, Desktop Pro) onto the dielectric. The insulation (or backing) is a 12.5-μm-thick layer of acrylic adhesive (DuPont, Pyralux FR1500) laminated to the electrode with heat and pressure.

Excess material for both footpad varieties was removed via laser machining (Oxford Lasers, E-Series), and both footpad varieties were bonded to the copper underside of the ankles (see the next section) with high-conductivity silver epoxy (MG Chemicals).

Leg fabrication

Like the robot's chassis, the legs (Fig. 2B) were also manufactured with the PC-MEMS process. Each leg is a seven-layer composite laminate that consists of two rigid layers, a flexural layer, and a conductive layer that was bonded together with three adhesive layers (DuPont, Pyralux FR1500). The rigid layers were formed by curing five layers of woven fiberglass (TenCate, YLA FB9K387) at 0°-45°-0°-45°-0° angles, and the cured fiberglass has a thickness of 100 μm. The flexural layer is a 7.5-μm-thick polyimide film (DuPont, Kapton), and the conductive layer for wiring electroadhesion signals to the footpads is a 5-μm conductive copper sheet.

Each layer was laser-machined (Oxford Lasers, E-Series), and then all layers were pin-aligned to cure the three adhesive layers under heat and pressure. A final laser machining step was performed on the cured laminate to separate the leg from support material. Last, the ankle joints were formed by gluing the assembly flexures in place with cyanoacrylate (Loctite 416).

Electroadhesive force measurements

The experimental setup in Fig. 7A was used to measure the electroadhesive force generated by circular electrodes and to characterize the static performance of the robot. The electrodes were connected in series to a low-stiffness spring and a micropositioning stage with a wire and positioned on an aluminum plate mounted on a three-axis force sensor (ATI, Nano17Ti). With adhesion active, the tension in the wire was gradually increased until the lateral force exerted on the active electrode (robot) exceeded the maximum shear force generated by electroadhesion. The normal adhesion force for the pads was then computed by using Eq. 2; however, we pulled in the normal direction to measure the robot's maximum normal load. The coefficients of friction for different electrodes on the aluminum substrate were measured with the same setup, with a control mass (m = 10 g) positioned on top of the electrodes. The effect of relative humidity (RH) on the resulting electroadhesive forces has been studied in previous work, and an increase of RH from 35 to 65% could lower the adhesion force by a factor of about 2 (*50*).

Blocked force measurements

The setup shown in Fig. 7B was used to measure the output shear force exerted by HAMR-E with electroadhesion active and inactive. The robot was placed on a horizontal aluminum substrate against a single-axis force sensor (Futek, LSB200). Tripedal crawl input signals of 240-V maximum amplitude and f = 0.2 Hz were used for actuation, and electroadhesion input voltages of 0 and 250 V were used for the inactive and active scenarios, respectively.

Motion tracking during inverted and vertical locomotion

The setup shown in Fig. 7C and described in (*25*) was used to track the robot during inverted locomotion experiments. Two high-speed cameras (Vision Research, Phantom v7.3) performed a stereo, 3D reconstruction of three markers on the body. The position of these markers was then used to estimate the position and orientation of the body. The spatial resolution of the setup is about 50 μm. To position HAMR-E in its inverted starting pose, we manually placed the robot on an aluminum plate, after which electroadhesion was activated. With the robot securely positioned on the substrate, the plane was rotated by 180°, after which the trial could begin. A similar camera setup was used to track vertical locomotion experiments and quantify the effective stride length (fig. S6).

Downloaded from https://www.science.org at The Hong Kong University of Science and Technology (Guangzhou) on May 26, 2026

SUPPLEMENTARY MATERIALS

robotics.sciencemag.org/cgi/content/full/3/25/eaau3038/DC1
Note S1. Cost of transport calculation.
Note S2. Charge accumulation measurements.
Fig. S1. Schematic of HAMR-E's SFB transmission.
Fig. S2. Electroadhesive force measurement details.
Fig. S3. Electrode manufacturing methods.
Fig. S4. Final swing and lift input waveforms.
Fig. S5. System-level diagram of the open-loop controller.
Fig. S6. Effective stride length during vertical locomotion.
Fig. S7. Electroadhesive pad characteristics.
Table S1. Tripedal crawl gait parameter values.
Table S2. Cost of transport for HAMR-E.
Movie S1. Inverted locomotion of HAMR-E.
Movie S2. Vertical locomotion of HAMR-E.
Movie S3. Inverted incline locomotion of HAMR-E.
Movie S4. Role of ankle joint during locomotion with adhesion.
Movie S5. Demonstration of inverted locomotion inside jet engine part.
Movie S6. Failure of HAMR-E during inverted locomotion when using a standard tripedal crawl gait.
Movie S7. Maneuverability of HAMR-E during locomotion with electroadhesion.

REFERENCES AND NOTES

1. K. Jayaram, R. J. Full, Cockroaches traverse crevices, crawl rapidly in confined spaces, and inspire a soft, legged robot. *Proc. Natl. Acad. Sci. U.S.A.* **113**, E950–E957 (2016).
2. B. L. Luk, D. S. Cooke, S. Galt, A. A. Collie, S. Chen, Intelligent legged climbing service robot for remote maintenance applications in hazardous environments. *Robot. Autonom. Syst.* **53**, 142–152 (2005).
3. W. Federle, M. Riehle, A. S. G. Curtis, R. J. Full, An integrative study of insect adhesion: Mechanics and wet adhesion of pretarsal pads in ants. *Integr. Comp. Biol.* **42**, 1100–1106 (2002).
4. K. Autumn, Y. A. Liang, S. T. Hsieh, W. Zesch, W. P. Chan, T. W. Kenny, R. Fearing, R. J. Full, Adhesive force of a single gecko foot-hair. *Nature* **405**, 681–685 (2000).
5. K. Autumn, A. Dittmore, D. Santos, M. Spenko, M. Cutkosky, Frictional adhesion: A new angle on gecko attachment. *J. Exp. Biol.* **209**, 3569–3579 (2006).
6. S. Kim, M. Spenko, S. Trujillo, B. Heyneman, D. Santos, M. R. Cutkosky, Smooth vertical surface climbing with directional adhesion. *IEEE Trans. Robot.* **24**, 65–74 (2008).
7. M. P. Murphy, C. Kute, Y. Mengüç, M. Sitti, Waalbot II: Adhesion recovery and improved performance of a climbing robot using fibrillar adhesives. *Int. J. Robot. Res.* **30**, 118–133 (2011).
8. O. Unver, A. Uneri, A. Aydemir, M. Sitti, Geckobot: A gecko inspired climbing robot using elastomer adhesives, in *Proceedings 2006 IEEE International Conference on Robotics and Automation (ICRA'06)* (IEEE, 2006), pp. 2329–2335.
9. Y. Li, A. Ahmed, D. Sameoto, C. Menon, Abigaille II: Toward the development of a spider-inspired climbing robot. *Robotica* **30**, 79–89 (2012).
10. M. Greuter, G. Shah, G. Caprari, F. Tache, R. Siegwart, M. Sitti, Toward micro wall-climbing robots using biomimetic fibrillar adhesives, in *Proceedings of the 3rd International Symposium on Autonomous Minirobots for Research and Edutainment (AMiRE'05)* (Springer, 2006), pp. 39–46.
11. E. W. Hawkes, D. L. Christensen, M. R. Cutkosky, Vertical dry adhesive climbing with a 100× bodyweight payload, in *2015 IEEE International Conference on Robotics and Automation (ICRA'15)* (IEEE, 2015), pp. 3762–3769.
12. W. A. Breckwoldt, K. A. Daltorio, L. Heepe, A. D. Horchler, S. N. Gorb, R. D. Quinn, Walking inverted on ceilings with wheel-legs and micro-structured adhesives, in *2015 IEEE/RSJ International Conference on Intelligent Robots and Systems (IROS'15)* (IEEE, 2015), pp. 3308–3313.
13. Z. Dai, S. N. Gorb, U. Schwarz, Roughness-dependent friction force of the tarsal claw system in the beetle *Pachnoda marginata* (Coleoptera, Scarabaeidae). *J. Exp. Biol.* **205**, 2479–2488 (2002).
14. C. J. Clemente, W. Federle, Pushing versus pulling: Division of labour between tarsal attachment pads in cockroaches. *Proc. Biol. Sci.* **275**, 1329–1336 (2008).
15. J. Zhu, D. Sun, S.-K. Tso, Development of a tracked climbing robot. *J. Intell. Robot. Syst.* **32**, 427–443 (2002).
16. H. Kim, D. Kim, H. Yang, K. Lee, K. Seo, D. Chang, J. Kim, Development of a wall-climbing robot using a tracked wheel mechanism. *J. Mech. Sci. Technol.* **22**, 1490–1498 (2008).
17. J. C. Grieco, M. Prieto, M. Armada, P. De Santos, A six-legged climbing robot for high payloads, in *Proceedings of the 1998 IEEE International Conference on Control Applications* (IEEE, 1998), vol. 1, pp. 446–450.
18. M. Eich, T. Vögele, Design and control of a lightweight magnetic climbing robot for vessel inspection, in *19th Mediterranean Conference on Control and Automation (MED'11)* (IEEE, 2011), pp. 1200–1205.
19. H. Wang, A. Yamamoto, T. Higuchi, Electrostatic-motor-driven electroadhesive robot, in *2012 IEEE/RSJ International Conference on Intelligent Robots and Systems* (IEEE, 2012), pp. 914–919.
20. R. Liu, R. Chen, H. Shen, R. Zhang, Wall climbing robot using electrostatic adhesion force generated by flexible interdigital electrodes. *Int. J. Adv. Robot. Syst.* **10**, 36 (2013).
21. H. Wang, A. Yamamoto, Analyses and solutions for the buckling of thin and flexible electrostatic inchworm climbing robots. *IEEE Trans. Robot.* **33**, 889–900 (2017).
22. D. Ruffatto, J. Shah, M. Spenko, Increasing the adhesion force of electrostatic adhesives using optimized electrode geometry and a novel manufacturing process. *J. Electrostat.* **72**, 147–155 (2014).
23. P. S. Sreetharan, J. P. Whitney, M. D. Strauss, R. J. Wood, Monolithic fabrication of millimeter-scale machines. *J. Micromech. Microeng.* **22**, 055027 (2012).
24. M. J. Spenko, G. C. Haynes, J. A. Saunders, M. R. Cutkosky, A. A. Rizzi, R. J. Full, D. E. Koditschek, Biologically inspired climbing with a hexapedal robot. *J. Field Robot.* **25**, 223–242 (2008).
25. B. Goldberg, N. Doshi, K. Jayaram, R. J. Wood, Gait studies for a quadrupedal microrobot reveal contrasting running templates in two frequency regimes. *Bioinspir. Biomim.* **12**, 046005 (2017).
26. B. F. Seitz, B. Goldberg, N. Doshi, O. Ozcan, D. L. Christensen, E. W. Hawkes, M. R. Cutkosky, R. J. Wood, Bio-inspired mechanisms for inclined locomotion in a legged insect-scale robot, in *2014 IEEE International Conference on Robotics and Biomimetics (ROBIO'14)* (IEEE, 2014), pp. 791–796.
27. B. Goldberg, R. Zufferey, N. Doshi, E. F. Helbling, G. Whittredge, M. Kovac, R. J. Wood, Power and control autonomy for high-speed locomotion with an insect-scale legged robot. *IEEE Robot. Autom. Lett.* **3**, 987–993 (2018).
28. N. T. Jafferis, M. J. Smith, R. J. Wood, Design and manufacturing rules for maximizing the performance of polycrystalline piezoelectric bending actuators. *Smart Mater. Struct.* **24**, 065023 (2015).
29. N. Doshi, B. Goldberg, R. Sahai, N. Jafferis, D. Aukes, R. J. Wood, Model driven design for flexure-based microrobots, in *IEEE/RSJ International Conference on Intelligent Robots and Systems (IROS'15)* (IEEE, 2015), pp. 4119–4126.
30. M. A. Graule, P. Chirarattananon, S. B. Fuller, N. T. Jafferis, K. Y. Ma, M. Spenko, R. Kornbluh, R. J. Wood, Perching and takeoff of a robotic insect on overhangs using switchable electrostatic adhesion. *Science* **352**, 978–982 (2016).
31. K. H. Koh, R. M. Kuppan Chetty, S. G. Ponnambalam, Modeling and simulation of electrostatic adhesion for wall climbing robot, in *2011 IEEE International Conference on Robotics and Biomimetics* (IEEE, 2011), pp. 2031–2036.
32. C. Cao, X. Sun, Y. Fang, Q.-H. Qin, A. Yu, X.-Q. Feng, Theoretical model and design of electroadhesive pad with interdigitated electrodes. *Mater. Design* **89**, 485–491 (2016).
33. M. H. Dickinson, C. T. Farley, R. J. Full, M. A. R. Koehl, R. Kram, S. Lehman, How animals move: An integrative view. *Science* **288**, 100–106 (2000).
34. G. C. Haynes, A. Khripin, G. Lynch, J. Amory, A. Saunders, A. A. Rizzi, D. E. Koditschek, Rapid pole climbing with a quadrupedal robot, in *IEEE International Conference on Robotics and Automation (ICRA'09)* (IEEE, 2009), pp. 2767–2772.
35. J. Clark, D. Goldman, P.-C. Lin, G. Lynch, T. Chen, H. Komsuoglu, R. J. Full, D. E. Koditschek, Design of a bio-inspired dynamical vertical climbing robot, paper presented at the 2007 Robotics: Science and Systems Conference, Atlanta, GA, 27 to 30 June 2007.
36. S. Kim, A. T. Asbeck, M. R. Cutkosky, W. R. Provancher, SpinybotII: Climbing hard walls with compliant microspines, in *Proceedings of the 12th International Conference on Advanced Robotics (ICAR'05)* (IEEE, 2005), pp. 601–606.
37. P. Ramdya, R. Thandiackal, R. Cherney, T. Asselborn, R. Benton, A. J. Ijspeert, D. Floreano, Climbing favours the tripod gait over alternative faster insect gaits. *Nat. Commun.* **8**, 14494 (2017).
38. Y. Chen, N. Doshi, B. Goldberg, H. Wang, R. J. Wood, Controllable water surface to underwater transition through electrowetting in a hybrid terrestrial-aquatic microrobot. *Nat. Commun.* **9**, 2495 (2018).
39. A. Yamamoto, T. Nakashima, T. Higuchi, Wall climbing mechanisms using electro-static attraction generated by flexible electrodes, in *International Symposium on Micro-NanoMechatronics and Human Science (MHS'07)* (IEEE, 2007), pp. 389–394.
40. H. Prahlad, R. Pelrine, S. Stanford, J. Marlow, R. Kornbluh, Electroadhesive robots- wall climbing robots enabled by a novel, robust, and electrically controllable adhesion technology, in *2008 IEEE International Conference on Robotics and Automation (ICRA'08)* (IEEE, 2008), pp. 3028–3033.
41. A. T. Baisch, O. Ozcan, B. Goldberg, D. Ithier, R. J. Wood, High speed locomotion for a quadrupedal microrobot. *Int. J. Robot. Res.* **33**, 1063–1082 (2014).
42. N. Doshi, K. Jayaram, B. Goldberg, Z. Manchester, R. J. Wood, S. Kuindersma, Contact-implicit optimization of locomotion trajectories for a quadrupedal microrobot, paper

Downloaded from https://www.science.org at The Hong Kong University of Science and Technology (Guangzhou) on May 26, 2026

presented at the 2018 Robotics: Science and Systems Conference, Pittsburgh, PA, 26 to 30 June 2018.
43. B. Goldberg, N. Doshi, K. Jayaram, J.-S. Koh, R. J. Wood, A high speed motion capture method and performance metrics for studying gaits on an insect-scale legged robot, in *2017 IEEE International Conference on Intelligent Robots and Systems (IROS'17)* (IEEE, 2017), pp. 3964–3970.
44. B. Goldberg, N. Doshi, R. J. Wood, High speed trajectory control using an experimental maneuverability model for an insect-scale legged robot, in *2017 IEEE International Conference on Robotics and Automation (ICRA'17)* (IEEE, 2017), pp. 3538–3545.
45. K. Jayaram, N. T. Jafferis, N. Doshi, B. Goldberg, R. J. Wood, Concomitant sensing and actuation for piezoelectric microrobots. *Smart Mater. Struct.* **27**, 481–486 (2018).
46. K. L. Hoffman, R. J. Wood, Robustness of centipede-inspired millirobot locomotion to leg failures, in *2013 IEEE/RSJ International Conference on Intelligent Robots and Systems (IROS'13)* (IEEE, 2013), pp. 1472–1479.
47. K. Jayaram, J.-M. Mongeau, A. Mohapatra, P. Birkmeyer, R. S. Fearing, R. J. Full, Transition by head-on collision: Mechanically mediated manoeuvres in cockroaches and small robots. *J. R. Soc. Interface* **15**, 20170664 (2018).
48. D. Ruffatto III, A. Parness, M. Spenko, Improving controllable adhesion on both rough and smooth surfaces with a hybrid electrostatic/gecko-like adhesive. *J. R. Soc. Interface* **11**, 20131089 (2014).
49. M. Karpelson, G.-Y. Wei, R. J. Wood, Driving high voltage piezoelectric actuators in microrobotic applications. *Sens. Actuators A Phys.* **176**, 78–89 (2012).
50. K.-J. Jeong, Y.-G. Park, Y.-S. Lee, T.-Y. Cho, H.-G. Chun, A study on the fabrication and characterization of alumina electrostatic chuck for silicon wafer processing. *J. Sens. Sci. Technol.* **8**, 481–486 (1999).
51. H. Wang, A. Yamamoto, T. Higuchi, A crawler climbing robot integrating electroadhesion and electrostatic actuation. *Int. J. Adv. Robot. Syst.* **11**, 191 (2014).
52. P. Birkmeyer, A. G. Gillies, R. S. Fearing, CLASH: Climbing vertical loose cloth, in *IEEE/RSJ International Conference on Intelligent Robots and Systems* (IEEE, 2011), pp. 5087–5093.

Acknowledgments: We would like to thank all members of the Harvard Microrobotics Laboratory for their advice and assistance. **Funding:** This work is partially funded by the Wyss Institute for Biologically Inspired Engineering and Rolls-Royce. In addition, the prototypes were enabled by equipment supported by the ARO DURIP program (award no. W911NF-13-1-0311). **Author contributions:** S.D.d.R., B.G., and R.J.W. initiated the project. S.D.d.R., B.G., N.D., and K.J. designed and conducted the research. J.Z. assisted with fabrication of the passive ankles. S.D.d.R., B.G., N.D., K.J., and R.J.W. contributed to the preparation of the manuscript. **Competing interests:** The authors declare that they have no competing interests. **Data and materials availability:** All data needed to evaluate the conclusions are included in the paper or the Supplementary Materials.

Submitted 30 May 2018
Accepted 24 November 2018
Published 19 December 2018
10.1126/scirobotics.aau3038

Citation: S. D. de Rivaz, B. Goldberg, N. Doshi, K. Jayaram, J. Zhou, R. J. Wood, Inverted and vertical climbing of a quadrupedal microrobot using electroadhesion. *Sci. Robot.* **3**, eaau3038 (2018).

Downloaded from https://www.science.org at The Hong Kong University of Science and Technology (Guangzhou) on May 26, 2026

Science Robotics

Inverted and vertical climbing of a quadrupedal microrobot using electroadhesion

Sébastien D. de Rivaz, Benjamin Goldberg, Neel Doshi, Kaushik Jayaram, Jack Zhou, and Robert J. Wood

Sci. Robot. **3** (25), eaau3038. DOI: 10.1126/scirobotics.aau3038

View the article online
https://www.science.org/doi/10.1126/scirobotics.aau3038
Permissions
https://www.science.org/help/reprints-and-permissions

Downloaded from https://www.science.org at The Hong Kong University of Science and Technology (Guangzhou) on May 26, 2026

Use of this article is subject to the Terms of service

Science Robotics (ISSN 2470-9476) is published by the American Association for the Advancement of Science. 1200 New York Avenue NW, Washington, DC 20005. The title *Science Robotics* is a registered trademark of AAAS.

Copyright © 2018 The Authors, some rights reserved; exclusive licensee American Association for the Advancement of Science. No claim to original U.S. Government Works